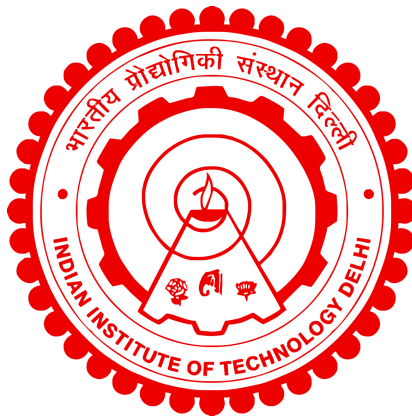


**UNRAVELING SPIN WAVE BEHAVIOR IN
ARTIFICIAL SPIN ICE AND
NON-COLLINEAR MAGNETIC TEXTURES**

NIMISHA ARORA



DEPARTMENT OF PHYSICS

INDIAN INSTITUTE OF TECHNOLOGY DELHI

JULY 2024

©Indian Institute of Technology Delhi (IITD), New Delhi, 2024

**UNRAVELING SPIN WAVE BEHAVIOR IN
ARTIFICIAL SPIN ICE AND
NON-COLLINEAR MAGNETIC TEXTURES**

by

NIMISHA ARORA

Department of Physics

Submitted

in fulfillment of the requirements of the degree of Doctor of Philosophy

to the



INDIAN INSTITUTE OF TECHNOLOGY DELHI

JULY 2024

*Dedicated to my family (Maa, Papa, and Bhai) and
Almighty*

ਮੇਰੇ ਪਰਿਵਾਰ (ਮਾਂ, ਪਾਪਾ ਅਤੇ ਭਰਾ) ਅਤੇ ਅਕਾਲ ਪੁਰਖ ਨੂੰ
ਸਮਰਪਿਤ

Certificate

This is to certify that the thesis entitled “**Unraveling of spin wave behavior in artificial spin ice and non-collinear magnetic textures**”, submitted by **Nimisha Arora** to the Indian Institute of Technology Delhi, for the award of the degree of **Doctor of Philosophy** in March 2024, is a record of the original, bonafide research work carried out by her under our supervision and guidance. The thesis has reached the standards fulfilling the requirements of the regulations related to the award of the degree.

The results in this thesis have not been submitted in part or in full to any other University or Institute for awarding any degree or diploma to the best of our knowledge.

Prof. Pintu Das

Department of Physics,
Indian Institute of Technology Delhi.
New Delhi-110016, India

Prof. Amartya Sengupta

Department of Physics,
Indian Institute of Technology Delhi.
New Delhi-110016, India

Acknowledgements

I extend my sincere gratitude to all those who have contributed to completing this Ph.D. thesis, directly or indirectly. This journey would not have been possible without your support, guidance, and encouragement.

First and foremost, I express my profound gratitude to my supervisor, Prof. Pintu Das, for his instrumental role in shaping my academic journey. Dr. Das introduced me to the captivating field of spin ice and instilled in me the confidence to navigate its complexities. His unwavering support, encouragement of new ideas, and willingness to engage in extensive academic discussions have been invaluable. Dr. Das's mentorship transcended mere guidance; he understood the ebbs and flows of my Ph.D. journey and took proactive steps to address any research hurdles that arose. Additionally, I thank him for broadening my research horizon through involvement in other research projects and assisting me with accommodations during the final phase of my thesis. I am deeply grateful for the invaluable lessons I have learned from Dr. Das, both academically and personally, which have profoundly shaped my growth as a researcher.

I am indebted to my co-supervisor, Prof. Amartya Sengupta, who has introduced me to the field of ultrafast optics and its applications. Initial discussions with him led me to investigate the spin wave aspects in artificial spin ice, which can be triggered using ultrafast laser pulses. His prompt responses to queries and academic discussions have been invaluable in my research journey.

I extend my heartfelt thanks to Dr. Neeti Keswani for her invaluable contribution to fabricating artificial spin ice samples. Special appreciation goes to Prof. Anjan Barman for graciously allowing me to conduct TR-MOKE studies in his lab at S.N. Bose National Centre for Basic Sciences (SNBNCBS), Kolkata, India, and for his insightful discussions and advice, which enhanced my understanding of magnetoelastic coupled modes in artificial spin ice lattices. I am grateful to Dr. Sourabh Sahoo and Kaustav for their assistance with TR-MOKE measurements and accommodation arrangements during my stay at SNBNCBS, Kolkata. I dedicate special thanks to Mr. Yogesh Kumar for engaging in academic discussions that extended my study into non-collinear magnetic textures and for his continuous support and friendship throughout my Ph.D. journey.

I express my appreciation to my research committee members, Prof. Ratnamala

Chatterjee, Prof. Sunil Kumar, and Prof. Sushma Santapuri, for their insightful questions, criticism, and wider perspectives, which enriched my research journey.

I acknowledge the Nanoscale Research Facility and the Department of Physics of the Indian Institute of Technology (IIT) Delhi, India, for providing fabrication and characterization facilities essential to this work. My deepest gratitude to the High Performance Computation facility of IIT Delhi for providing computational resources and to the supportive staff who assisted me in overcoming technical challenges. I would like to acknowledge the financial support provided by the Ministry of Science, which made it possible for me to focus on my research without the burden of financial constraints.

I am immensely grateful to all my lab members, including Dr. Neeti, Hural, Yogesh, Neesha, Sandeep, Subhrojyoti, Sreelekshmi, Dr. Harish, Dr. Amodini, and Nilesh, who have been integral parts of my Ph.D. journey, offering unwavering camaraderie, engaging in stimulating academic discussions, and fostering a conducive environment for both research and personal growth. Their collective efforts have enriched my experience and contributed significantly to realizing my academic goals. I extend my heartfelt appreciation to my friends for their steadfast support and for adding beauty to this journey with their companionship. In particular, I wish to express my sincere gratitude to Hardeep, whose presence during challenging times served as a source of upliftment and invaluable encouragement.

Last but certainly not least, my deepest gratitude goes to my family, whose steadfast strength, constant encouragement, understanding, and belief in my abilities have been my pillars of strength. I owe a debt of gratitude that words cannot adequately express to my late father, Mr. Dharamveer Arora, whose vision ignited my passion for advanced scientific endeavors. I am profoundly thankful to my mother, Ms. Poonam Arora, for her consistent support and for instilling in me an unwavering trust in my capabilities. I extend my heartfelt appreciation to my brothers, Mr. Sidhant Arora and Mr. Khushal Arora, for being the strongest pillars in my life and for their unwavering presence and support in every conceivable way. Their love and support have been the cornerstone of my journey, and I am eternally grateful for that.

Thank you all for your invaluable contributions.

Nimisha Arora

Abstract

Magnonics, a burgeoning field within nanomagnetism, focuses on utilizing spin waves (SW) or magnons for information transmission, storage, and processing. Magnonic crystals, typically composed of periodic and aperiodic arrangements of nanomagnetic entities with varying shapes, sizes, and materials, can be tailored to explore unique properties such as negative group velocity, anisotropic dispersion relation, nonreciprocity, and reconfigurability. These properties hold promise for developing next-generation information processing and storage technologies. To create reconfigurable magnonic devices, precise control over SW behavior and seamless integration with spintronic and electronic systems are essential. Artificial spin ice (ASI) and non-collinear magnetic textures emerge as promising candidates for achieving these objectives. ASI consists of engineered arrays of dipolar-coupled single-domain ferromagnetic nanomagnets, mimicking frustrated spins found in rare earth titanate pyrochlores like $\text{Ho}_2\text{Ti}_2\text{O}_7$ and $\text{Dy}_2\text{Ti}_2\text{O}_7$. Originally designed for studying geometrically induced magnetic frustration, phase transitions, and emergent magnetic monopoles, these structures offer multiple degenerate microstates, enabling the manipulation of SW excitations. Despite recent interest in SW behavior within these arrays and clusters of dipolar-coupled nanomagnets, a comprehensive understanding of SW excitation, propagation, and its coupling with other excitations in the presence of emergent magnetic monopole and bound monopole-polaron states remains elusive. Additionally, non-collinear magnetic textures such as radial vortex, skyrmions, etc., arising from the intricate interplay of fundamental magnetic interactions, including symmetric Heisenberg exchange, perpendicular anisotropy, and antisymmetric Dzyaloshinskii-Moriya (DM) interaction, offer advantages over simpler counterparts like nanomagnets with single-domain states in terms of reconfigurable magnonics. The SW excitations in these textures feature shorter wavelengths, non-linearity, and non-reciprocity. Exploring these properties involves stabilizing novel textures across diverse magnetic and geometrical parameter ranges and investigating their corresponding SW responses.

In this thesis, we provide an in-depth analysis of SW behavior in the building block of square ASI, finite-size square ASI, and square ASI array using micromagnetic simulations and Time-resolved magneto-optic Kerr effect (TR-MOKE) spectroscopy. We delve into the influence of magnetoelastic coupling on SWs, through the concurrent

excitation of phonons induced by laser pulse irradiation on the square ASI array using TR-MOKE spectroscopy. Finally, we explore the non-trivial SW behavior in a novel non-collinear magnetic texture within a confined nanodisk with interfacial DM interaction.

Firstly, we investigated the collective SW response in the square ASI and its building blocks using micromagnetic simulations. Our study reveals key features associated with magnetization reversal in constituent nanomagnets during the evolution of microstates at varying external magnetic fields in the respective excited SW spectra. Analysis of the spatial distribution of power profiles associated with excited SW modes shows the significant influence of local magnetic charges, i.e., local converging and diverging magnetic flux lines, in the inhibition and facilitation of specific SW modes. Our comprehensive analyses of the building block and square ASI structure demonstrate that the collective excitation of SWs and their behavior in square ASI can be understood by examining their corresponding building blocks. Further, we demonstrate that limited efficient and anisotropic transmission of SWs can occur between nanomagnets solely due to the dipolar interaction inherent in square ASI configurations. Our study underscores the critical role of local magnetic charges in facilitating this anisotropic transmission of SWs to neighboring nanomagnets when a spatially localized magnetic field perturbation is applied at the magnetically uncharged vertex. Our findings reveal distinctive features in the spectral attributes of SWs when magnetically charged states, such as emergent magnetic monopoles and anti-monopoles, and bound monopole-polaron states, are present within finite-size square ASI systems.

Based on our simulation findings, we explore the collective SW response in a square ASI lattice using TR-MOKE spectroscopy. Here, we employ a highly focused pump pulse to excite a single ASI vertex during irradiation. Our experimental investigation reveals that in large arrays of such ASI vertices, viz., square ASI lattice, magnetoelastic coupling emerges as a critical factor influencing the collective SW response. Magnetoelastic coupling arising due to the concurrent excitation of phonon modes through pump pulse irradiation results in the observation of non-dispersive SW modes, which are independent of the magnetic field due to magnetoelastic coupling. We show that the influence of magnetoelastic coupling can be tuned by controlling the underlying magnetic state through external magnetic orientation relative to lattice symmetry or by introducing defects like misaligned nanomagnets to break the

symmetry of the square ASI lattice. To corroborate our experimental findings, we employ a multistep modeling approach to simulate coupled magnetoelastic modes induced by ultrafast laser pulse irradiation on square ASI samples. Details of the multi-step model and its outcomes are presented alongside the experimental findings.

Finally, we present our analysis of SW modes in non-collinear magnetic textures by conducting detailed micromagnetic simulations in Co/Pt bilayer nanodisks. The simulated ferromagnetic/non-magnetic bilayer nanodisks exhibit interfacial DM interaction, thereby facilitating the stabilization of non-collinear magnetic textures with specific chirality. Our study demonstrates the stabilization of a novel magnetic texture through a series of magnetic texture transitions induced by sweeping an external magnetic field. The SW studies conducted in these textures highlight the non-reciprocal nature of the excited SW mode, which is exclusively observed in the novel texture. Furthermore, our study demonstrates efficient switching of this novel state into a target-skyrmion state within a few nanoseconds timescales by resonating the equilibrium magnetic state at the eigenfrequency of its radial SW mode. This finding holds promise for developing power-efficient spintronic memory devices.

सारांश

मैग्रोनिक्स, जो नैनोमैग्नेटिज्म के भीतर एक उभरता हुआ क्षेत्र है, सूचना प्रसारण, भंडारण और प्रसंस्करण के लिए स्पिन तरंगों (SW) या मैग्रॉन्स का उपयोग करने पर केंद्रित है। मैग्रॉनिक क्रिस्टल, जो आमतौर पर विभिन्न आकारों, आयामों, और सामग्रियों के नैनोमैग्नेटिक इकाइयों की आवधिक और गैर-आवधिक व्यवस्थाओं से बने होते हैं, अद्वितीय गुणों जैसे नकारात्मक समूह वेग, अनिसोट्रॉपिक डिस्पर्शन संबंध, गैर-अनुप्रत्यास्था, और पुनः संयोजनीयता का पता लगाने के लिए अनुकूलित किए जा सकते हैं। ये गुण अगली पीढ़ी की सूचना प्रसंस्करण और भंडारण प्रौद्योगिकियों के विकास के लिए महत्वपूर्ण हैं। पुनः संयोजन योग्य मैग्रोनिक उपकरण बनाने के लिए, SW व्यवहार पर सटीक नियंत्रण के अलावा स्पिनट्रॉनिक और इलेक्ट्रॉनिक सिस्टम के साथ समेकित एकीकरण आवश्यक है।

आर्टिफिशियल स्पिन आइस (ASI) और गैर-कोलीनियर मैग्नेटिक टेक्सचर इन लक्ष्यों को प्राप्त करने के लिए आशाजनक विकल्प के रूप में उभर रहे हैं। ASI डायपोलर-कपलड सिंगल-डोमेन फेरोमैग्नेटिक नैनोमैग्नेट्स की इंजीनियर्ड श्रृंखलाओं से बना होता है, जो $\text{Ho}_2\text{Ti}_2\text{O}_7$ और $\text{Dy}_2\text{Ti}_2\text{O}_7$ जैसे दुर्लभ पृथ्वी टाइटेनेट पायरोक्लोर्स में पाए जाने वाले फ्रस्ट्रेटेड स्पिनो की नकल करते हैं। सामान्यतः ज्यामितीय रूप से प्रेरित चुंबकीय फ्रस्ट्रेशन, फेज ट्रांज़िशन, और उभरते हुए चुंबकीय मोनोपोल्स का अध्ययन करने के लिए डिज़ाइन की गई इन संरचनाओं में कई समान ऊर्जा वाले माइक्रोस्टेट्स होते हैं, जो SW उत्तेजनाओं के नियंत्रण को सक्षम बनाते हैं।

हाल ही में इन डायपोलर-कपलड नैनोमैग्नेट्स के समूहों और क्लस्टरों में SW व्यवहार में रुचि के बावजूद, उभरते हुए चुंबकीय मोनोपोल और बाउंड मोनोपोल-पोलारॉन अवस्थाओं की उपस्थिति में SW उत्तेजना, प्रसार और अन्य उत्तेजनाओं के साथ उसके संयोजन की व्यापक समझ अब भी अधूरी है। इसके अतिरिक्त, सममित हाइजेनबर्ग एक्सचेंज, लंबवत एनिसोट्रॉपी (असमदिग्वर्ती होने की दशा), और असममित डेज़्यालोशिंस्की-मोरिया (DM) इंटरैक्शन जैसी मौलिक चुंबकीय अंतःक्रियाओं के जटिल समन्वय से उत्पन्न गैर-कोलीनियर चुंबकीय संरचनाएं जैसे कि रेडियल वॉर्टेक्स, स्किर्मियॉन्स आदि, एकल-डोमेन अवस्थाओं वाले साधारण नैनोमैग्नेट्स की तुलना में पुनः संयोजनीय मैग्रोनिक्स के लिए अधिक लाभकारी हैं। इन संरचनाओं की SW उत्तेजनाओं में छोटे तरंगदैर्घ्य, गैर-रैखिकता, और गैर-अनुप्रत्यास्था जैसी विशेषताएं होती हैं। इन गुणों का अन्वेषण करने के लिए विभिन्न चुंबकीय और ज्यामितीय मापदंडों की सीमा में नई संरचनाओं को स्थिर करना और उनके संबंधित SW प्रतिक्रियाओं की जांच करना शामिल है।

इस शोध प्रबंध में, हम माइक्रोमैग्नेटिक सिमुलेशन और टाइम-रिज़ॉल्व्ड मैग्नेटो-ऑप्टिक केर्र इफेक्ट (TR-MOKE) स्पेक्ट्रोस्कोपी का उपयोग करके स्क्वायर ASI के बिल्डिंग ब्लॉक, सीमित आकार के स्क्वायर ASI, और स्क्वायर ASI सरणी में SW व्यवहार का गहन विश्लेषण प्रदान करते हैं। हम TR-MOKE स्पेक्ट्रोस्कोपी

का उपयोग करके लेजर पल्स विकिरण द्वारा स्क्वायर ASI सरणी पर प्रेरित फॉनॉन (ध्वनि-कण) की सह उत्तेजना के माध्यम से SW पर मैग्नेटोइलास्टिक कपलिंग के प्रभाव का विश्लेषण करते हैं। अंत में, हम इंटरफेसियल DM इंटरैक्शन के साथ सीमित नैनोडिस्क में एक नवीन गैर-कोलीनियर मैग्नेटिक टेक्सचर में जटिल SW व्यवहार का पता लगाते हैं।

सबसे पहले, हमने माइक्रोमैग्नेटिक सिमुलेशन का उपयोग करके स्क्वायर ASI और इसके बिल्डिंग ब्लॉक्स में सामूहिक SW प्रतिक्रिया की जांच की। हमारा अध्ययन विभिन्न बाहरी मैग्नेटिक क्षेत्रों में माइक्रोस्टेट्स के विकास के दौरान घटक नैनोमैग्नेट्स में चुंबकत्व उलट के साथ जुड़े प्रमुख विशेषताओं का खुलासा करता है, जो संबंधित उत्तेजित SW स्पेक्ट्रा में दिखाई देती हैं। उत्तेजित SW मोड्स से संबंधित पावर प्रोफाइल के स्थानिक वितरण का विश्लेषण यह दर्शाता है कि विशिष्ट SW मोड्स की अवरोधन और सुविधा में स्थानीय चुंबकीय चार्जेंस, यानी स्थानीय कन्वर्जिंग और डाईवर्जिंग चुंबकीय फ्लक्स लाइनों का महत्वपूर्ण प्रभाव होता है। निर्माण खंड और स्क्वायर ASI संरचना के हमारे व्यापक विश्लेषण यह दर्शाते हैं कि SWs की सामूहिक उत्तेजना और उनका व्यवहार स्क्वायर ASI में उनके संबंधित निर्माण खंडों की जांच करके समझा जा सकता है।

आगे, हमने प्रदर्शित किया कि स्क्वायर ASI वर्टेक्स में केवल डाईपोलर अंतःक्रिया के कारण नैनोमैग्नेट्स के बीच सीमित एनिसोट्रॉपिक SW ट्रांसमिशन हो सकता है। हमारा अध्ययन यह बताता है कि स्थानीय चुंबकीय चार्जेंस की महत्वपूर्ण भूमिका होती है जब एक स्थानिक रूप से स्थानीयकृत चुंबकीय क्षेत्र विक्षोभ (perturbation) को अनचार्ज वर्टेक्स पर लागू किया जाता है, तब SWs का यह एनिसोट्रॉपिक ट्रांसमिशन पड़ोसी नैनोमैग्नेट्स में होता है। हमारे निष्कर्ष यह प्रकट करते हैं कि जब चुंबकीय रूप से चार्ज्ड अवस्थाएं, जैसे कि उभरते चुंबकीय मोनोपोल और एंटी-मोनोपोल, और बाउंड मोनोपोल-पोलारॉन अवस्थाएं, सीमित आकार के स्क्वायर ASI सिस्टम्स में उपस्थित होती हैं तब SWs के स्पेक्ट्रल गुणों में विशिष्ट विशेषताएं होती हैं।

हमारे सिमुलेशन निष्कर्षों के आधार पर, हम TR-MOKE स्पेक्ट्रोस्कोपी का उपयोग करके स्क्वायर ASI लैटिस में सामूहिक SW प्रतिक्रिया की जांच करते हैं। यहाँ, हम एक अत्यधिक केंद्रित पंप पल्स का उपयोग करके एकल ASI वर्टेक्स को उत्साहित करते हैं। हमारे प्रयोगात्मक अध्ययन से पता चलता है कि ऐसे ASI वर्टेक्स के बड़े समूहों, यानी स्क्वायर ASI लैटिस में, मैग्नेटोइलास्टिक कपलिंग सामूहिक SW प्रतिक्रिया को प्रभावित करने वाला एक महत्वपूर्ण कारक बनकर उभरता है। पंप पल्स विकिरण के माध्यम से फॉनॉन (ध्वनि-कण) मोड्स की समवर्ती उत्तेजना के कारण उत्पन्न मैग्नेटोइलास्टिक कपलिंग के कारण गैर-प्रसारक SW मोड्स का अवलोकन होता है, जो मैग्नेटोइलास्टिक कपलिंग के कारण चुंबकीय क्षेत्र पर निर्भर नहीं होते हैं। हम यह दिखाते हैं कि स्क्वायर ASI लैटिस की सममिति को तोड़ने के लिए बाहरी चुंबकीय अभिविन्यास के माध्यम से या गलत संरेखित नैनोमैग्नेट्स जैसे दोषों को प्रस्तुत करके अंतर्निहित चुंबकीय अवस्था को नियंत्रित करके मैग्नेटोइलास्टिक कपलिंग के प्रभाव को समायोजित किया जा सकता है। हमारे प्रयोगात्मक निष्कर्षों की पुष्टि करने के लिए, हम स्क्वायर ASI नमूनों पर अल्ट्राफास्ट लेजर पल्स विकिरण द्वारा प्रेरित

युग्मित मैग्नेटोइलास्टिक मोड्स का अनुकरण करने के लिए एक बहु-चरणीय मॉडलिंग दृष्टिकोण का उपयोग करते हैं। बहु-चरणीय मॉडल और इसके परिणामों का विवरण प्रयोगात्मक निष्कर्षों के साथ प्रस्तुत किया गया है।

अंत में, हम Co/Pt बाइलेयर नैनोडिस्क में विस्तृत माइक्रोमैग्नेटिक सिमुलेशन करके, गैर-कोलीनियर चुंबकीय संरचनाओं में SW मोड्स का विश्लेषण प्रस्तुत करते हैं। सिमुलेटेड फेरोमैग्नेटिक/गैर-चुंबकीय बाइलेयर नैनोडिस्क इंटरफेशियल DM इंटरैक्शन प्रदर्शित करते हैं, जिससे विशिष्ट काइरैलिटी के साथ गैर-कोलीनियर चुंबकीय संरचनाओं की स्थिरीकरण सुविधा मिलती है। हमारा अध्ययन यह दर्शाता है कि बाहरी चुंबकीय क्षेत्र को बदलकर एक श्रृंखला के चुंबकीय संरचना संक्रमणों के माध्यम से एक नई चुंबकीय संरचना को स्थिर किया जा सकता है। इन संरचनाओं में किए गए SW अध्ययन यह उजागर करते हैं कि उत्तेजित SW मोड की गैर-पारस्परिक प्रकृति विशेष रूप से नई संरचना में देखी जाती है। इसके अतिरिक्त, हमारा अध्ययन यह दिखाता है कि इस नई अवस्था को कुछ नैनोसेकंड के समय अंतराल में टार्गेट-स्किर्मियन अवस्था में प्रभावी रूप से स्विच किया जा सकता है, जब इसके रेडियल SW मोड की स्व-आवृत्ति पर संतुलन चुंबकीय अवस्था को अनुनादित किया जाता है। यह निष्कर्ष पावर-प्रभावी स्पिंट्रॉनिक मेमोरी डिवाइसों के विकास के लिए संभावनाएं प्रस्तुत करता है।

Contents

Certificate

Acknowledgements

Abstract

Contents

List of Figures

List of Tables

Abbreviations

Symbols

1	Introduction	1
1.1	Artificial spin ice (ASI)	2
1.2	Non-collinear magnetic textures	8
1.3	Motivation	13
1.4	Overview of the thesis	15
1.5	Micromagnetism	16
1.5.1	Magnetization vector	17
1.5.2	Landau-Lifshitz-Gilbert (LLG) equation	17
1.5.3	Free energy	18
1.5.4	Zeeman energy	20
1.5.5	Exchange energy	20
1.5.6	Bilinear exchange energy	22
1.5.7	Magnetic dipolar energy	23
1.5.8	Anisotropy energy	24

1.6	Kittel mode	27
1.7	Magneto-optic Kerr effect	30
1.8	Theory of linear elasticity	32
1.9	Magnetoelastic effect	33
1.9.1	Magnetoelastic energy	33
1.9.2	Effective field approach	35
1.10	Summary	36
2	Experimental and simulation techniques	37
2.1	Electron Beam Lithography (EBL)	37
2.1.1	Key components of an EBL system	38
2.1.2	Operational mechanism of EBL system	41
2.2	Atomic Force Microscopy (AFM)	42
2.3	Magnetic Force Microscopy (MFM)	45
2.4	Scanning Electron Microscopy (SEM):	46
2.5	Energy Dispersive X-ray Spectroscopy (EDS/EDX)	47
2.6	Electron Beam Deposition system (EBD)	49
2.7	Superconducting Quantum Interference Device (SQUID) magnetometry	50
2.8	Time-Resolved Magneto-Optic Kerr Effect (TR-MOKE) spectroscopy	51
2.8.1	Pump excitation mechanism	53
2.8.1.1	Three-temperature model	54
2.8.1.2	Thermal anisotropy pulse	55
2.8.2	Excitation geometry consideration	57
2.8.3	Time domain analysis	58
2.9	Micromagnetic simulations	60
2.9.1	MuMax3: A micromagnetic simulator	60
2.9.2	Power & phase profiles	63
2.10	Multistep magnetoelastic modelling approach	64
2.10.1	Modelling of temperature rise	65
2.10.2	Modelling of surface acoustic waves	69
2.10.3	Modelling of magnetoelastic modes	69
3	Role of dipolar interaction in the collective spin wave excitation in square artificial spin ice and it's building block	73
3.1	Introduction	74
3.2	Spin wave modes in individual nanomagnet	77
3.3	Spin wave modes in dipolar coupled E-and H- nanomagnets	82
3.4	Analysis of spin wave behavior in square ASI and its building block	84
3.4.1	Magnetization reversal in dipolar coupled ring type structures	84
3.4.2	Spin wave modes in saturated state ($\mu_0 H_{\text{ext}}=250$ mT)	89
3.4.3	Spin wave modes in remnant state	91
3.4.4	Spin wave modes in state-(i)	96

3.4.5	Spin wave modes in state-(ii)	101
3.5	Conclusion	105
4	Spin waves in emergent magnetic monopole and monopole-polaronic environment in finite-size artificial spin ice	107
4.1	Introduction	108
4.2	SW modes in OE vertex	112
4.2.1	Saturated state	112
4.2.2	Remanent state	118
4.2.2.1	Dependence on initial magnetic field direction	127
4.2.3	SW mode ‘propagation’ in square ASI array	135
4.3	SW behavior in presence of monopole-polaron environment	139
4.3.1	Dependence of SW modes on the strength of external magnetic field	143
4.4	Conclusion	148
5	Investigation of magnetoelastic coupling in spin wave dynamical behavior of artificial spin ice lattice	149
5.1	Introduction	150
5.2	Magnon and phonon modes in artificial spin ice	153
5.2.1	Dispersion of dynamical modes with magnetic field’s strength	156
5.2.2	Simulated magnetoelastic modes in square ASI geometry	166
5.2.3	Tuning of magnetoelastic modes	175
5.3	Conclusion	186
6	Spin wave behavior in novel non-collinear magnetic state	187
6.1	Introduction	188
6.2	Stabilization of novel non-collinear magnetic state	192
6.3	Spin waves in non-collinear magnetic textures	200
6.3.1	Switching of non-collinear magnetic states via SW modes	213
6.3.2	Dispersion of SW modes with external magnetic field	216
6.4	Conclusion	218
7	Major outcomes & scope for Future work	219
7.1	Major outcomes of the thesis	219
7.2	Scope for Future Work	223
A	Micromagnetic simulation of SW modes in square ASI geometry	229
A.1	MuMax3 code for simulation of SW modes in OE vertex using localized excitation	229
A.2	MuMax3 code for simulation of SW modes in imported SEM geometry	233

A.3	MuMax3 code for simulation of SW modes in square ASI geometry with exact dimensions	234
A.4	MuMax3 code for simulation of ME modes in square ASI geometry	237
B	Matlab codes for SW modes' power and phase profiles	247
B.1	Creating mat format file from multiple *.ovf files	247
B.2	Matlab code to generate SW mode spectra and mode power profile from the mat file	254
	Bibliography	259
	List of Publications	283
	Biography	285

List of Figures

1.1	(a) Schematic of square artificial spin ice with representative macrospins alignment. The inset in the top right corner shows the zoomed image of the macrospins arrangement in an individual vertex. (b) Schematic of possible degenerate macrospin configurations at the vertex in square artificial spin ice, categorized as Type-I, Type-II, Type-III, and Type-IV. Type-III and Type-IV exhibit local converging and diverging magnetic flux, identified as local magnetic charges ($\pm Q_m$, $\pm 2Q_m$), which are depicted with colored circular discs at the vertex center and also shown above the schematic.	3
1.2	(a) Simulated square artificial spin-ice lattice with monopole-antimonopole pairs connected by Dirac strings. (b) Simulated resonance spectra with increasing length of Dirac string connected to monopole-antimonopole pairs. The spectrum for reference state is shown using the gray-filled area in (a). Adapted from [1]. (c) Simulated edge mode amplitudes for the e-I and e-II vertices. Top: The square lattice possesses two possible degenerate configurations (labeled e-I and e-II) of the magnetization. The two configurations e-I and e-II have a single magnetic symmetry axis (red arrow). Bottom: Spectra for a lattice composed of different numbers of e-I-type and e-II vertices. Adapted from [2].	4
1.3	(a) Scanning electron micrograph ($3.5 \times 3.5 \mu m^2$) of ASVI. The permalloy bars are 600 nm long, 200 nm (wide bar) or 125 nm (thin bar) wide and 20 nm thick, with a 100 nm vertex gap (bar end to vertex center). (b) MFM series of 0–30 ± 18 mT field cycle states imaged after application of negative (top row) and positive (bottom row) fields of each field cycle. (c) Differential ± 10 mT FMR heatmaps measured after 0, 3, 10, and 30 ± 18 mT field cycles. (d, e) Future prediction of $t+1$ (d) and $t+10$ (e) for a Mackey–Glass chaotic differential time series, a commonly used reservoir computing benchmark. ASVI performs well while raw inputs fail to produce a true prediction, simply reproducing the input dataset with a $t+1$ time lag (d), failing badly at the more challenging $t+10$ task (e). Adapted from [3]	7

1.4	Schematic of (a) Bloch (Vortex) skyrmion and (b) Néel (Hedgehog) skyrmion, adapted from [4]. (c) Schematic representing chiral domain wall in ferromagnetic/normal metal heterostructure, adapted from [5]. (d) Typical structure of Toroidal hopfion with Hopf index $H = 1$. The solid-colored isolines connect points r of a vector field $\mathbf{n}(r) = (\cos\phi\sin\theta, \sin\phi\sin\theta, \cos\theta)$ with fixed values of angular variables, $\theta \equiv \theta(r)$ and $\phi \equiv \phi(r)$. (e) The texture of toroidal hopfion at intersecting planes $z = 0$ and $x = 0$, respectively. Adapted from [6]	10
1.5	(a) Resonance frequencies of distinct chiral textures emerging as a ground state in the ultrathin magnetic circular dot of the radius $R = 125$ nm and thickness $t = 1.4$ corresponding to material parameters of CoFeB-MgO heterostructure as a function of varying uniaxial anisotropy and DM coefficient when an external Sinc pulse is applied along the out-of-plane, i.e., z -axis (top panel) and in-the-plane, i.e., x -axis (middle panel) of the nanodisk. The SW excitations in a single domain ground state are indicated with solid white dotted and dashed lines. The static properties of the solitons are presented by the skyrmion number (S_{no}) and skyrmion phase (ϕ°), bottom two panels. Adapted from [7]. As the chiral state changes, the behavior of SW modes changes with K_u and D , showing the tunability of complex SW response. (b) Nonreciprocal propagation in a thin rectangular wire shown by the spatial profile of m_x , resulting from an rf field excitation of field amplitude 5 mT and frequency 50 GHz. (c) Simulated dispersion relation computed for (b) when $D_{ex} = 4.5$ mJ/m ² . Dots represent simulation results while the solid black curve (and gray shaded area) represents the theoretical dispersion relation for exchange modes, adapted from [8] (d-f) SW-Based XNOR Logic Gate: (d) Domain structure of the 2×2 network with two inputs and one output. (e) The truth table of the XNOR logic gate is based on the exchange SW in the chiral domain wall. (f) Time-dependent magnetization component (M_z) in the domain wall center underneath the output nanowires with four input logics. Adapted from [9]	11
1.6	(a) The Landau-Lifshitz equation governs the rotation of the magnetization vector around the effective field, \mathbf{H}_{eff} , whereas (b) the Landau-Lifshitz-Gilbert equation describes the precession of the magnetization vector and incorporates a phenomenological damping term, α , in the direction $\mathbf{M} \times \frac{d\mathbf{M}}{dt}$	19
1.7	Exchange constant terms for different crystallographic structures . . .	22
1.8	Schematic illustrating the transition from multidomain to single domain structure in a ferromagnetic material as the size of nanoparticles decreases.	27
1.9	Schematic of various Kerr effect configurations: (a) Polar configuration, (b) Longitudinal configuration, and (c) Transverse configuration.	30

2.1	Schematic representation of an electron beam column.	39
2.2	Schematic representation of positive and negative resist.	42
2.3	Schematic of the AFM system	43
2.4	Schematic showing the resonance shift during tapping mode.	44
2.5	Schematic diagram of X-ray emission from an atom	48
2.6	Schematic of the electron beam vapor deposition system.	50
2.7	Schematic of (a) SQUID's working circuit, and (b) superconducting pick-up coil.	51
2.8	Schematic diagram of an all-optical TR-MOKE spectroscopy with collinear pump-probe geometry. Here, the annotations in the schematic are as follows: MR & MB: reflecting mirrors in the optical path of the probe (red arrow) and pump (blue arrow) beams, B: beam-splitter, A: attenuator, L: lens, OBD: optical bridge detector, MO: microscope objective, G: glass slide, FR & FB: spectral filters, and DPSS: diode-pumped solid-state laser.	53
2.9	(a) Schematic showing the interaction between the electron, lattice, and spin baths and (b) an example of the time evolution of the different subsystems governed by the rate eqs. 2.7. The red line corresponds to the excitation laser pulse. The subscripts e, l, and s correspond to the electron, lattice, and spin systems, respectively. The evolution of the spin system is shown for a metal (blue dotted line) and a dielectric (blue dashed line). Taken from [10]	55
2.10	Schematic illustrating the impact of a thermal pulse as an excitation mechanism for magnetization precession at (a) $t < 0$, i.e., before pulse incidence, (b) $0 < t < t_{eq}$, i.e., after pulse incidence, and (c) $t > t_{eq}$, i.e., after systems cool.	56
2.11	Precessional and excitation characteristics of a thin film with an in-plane easy axis. (a) When the magnetization is aligned perpendicular to the surface due to a strong external magnetic field, (b) When the magnetization aligns along the easy axis, and (c) If the magnetization is canted relative to the easy axis.	58
2.12	Raw TR-MOKE signal from a reference permalloy film with $H_{ext}=200$ mT and $\theta_H = 10^\circ$. At $t = 0$, the pump pulse excites the system, leading to rapid changes in the signal due to heating and demagnetization. On a slower timescale, the magnetization undergoes precession around the effective field. Some residual heat in the system is evident as a slowly decaying backdrop to the oscillation (depicted by the red line). (b) Subtracting this slowly decaying backdrop from the raw signal isolates the pure dynamical motion described by the LLG equation. (c) The FFT algorithm transforms the time signal into the frequency domain power spectrum.	59
2.13	Staircase effect in discretized nanodisc geometry in FDM based micromagnetic solver: MuMax3.	62

2.14	Temporal square-shaped magnetic field pulse employed for triggering SW modes in nanomagnets.	62
2.15	Hierarchy of operations performed by MATLAB script to post-process the output *.OVF files.	64
2.16	(a) Simulated ASI geometry used for solving coupled 3-temperature model in FEM-based COMSOL Multiphysics. (b) Physical controlled Free tetrahedral and triangular meshing in the simulated ASI geometry,	66
2.17	(a) Spatial and (b) temporal pulse shape of indecent ultrafast laser employed to trigger surface acoustic waves.	66
2.18	(a-c) Snapshots of COMSOL Multiphysics interface showing the input heat sources in the three different heat transfer physics prompt, loaded for each electron, phonon, and spin baths.)	68
2.19	Snapshots of COMSOL Multiphysics interface showing the time-dependent solver settings in (a) three coupled heat transfer physics modules and (b) coupled heat transfer module for lattice and solid mechanics module for resultant strain in the system.	70
3.1	Schematic representation of (a) an individual nanomagnet and dipolar-coupled nanomagnets arranged in (b) a single square ring, (c) double rings, (d) triple rings, (e) quadruple rings (square ASI), and (f) diagonal-double rings geometry are depicted. Dimensions of the individual nanomagnet and lattice constant (edge-to-edge) are indicated in the figure.	76
3.2	(a) Time response of the z-component of magnetization (m_z) following transient magnetic field excitation on the E-nanomagnet at saturation ($\mu_0 H_{\text{ext}} = 250$ mT). (b) Power spectra obtained through Fast Fourier Transform (FFT) of the time evolution of m_z . (c) Spatial distribution of FFT power for the excited SW (SW) modes at saturation. The colorbar on the right of (b) quantifies the magnetization along the x-axis, while the colorbars on the right of (c) quantify the SW power and phase distributed within the nanomagnet.	78
3.3	(a) Time response of z-component of magnetization (m_z) after transient magnetic field excitation on H-nanomagnet at saturation ($\mu_0 H_{\text{ext}} = 250$ mT), (b) FFT power spectra of recorded $m_z(t)$. The inset shows the internal spin configuration at saturation. (c) spatial distribution of FFT power in logarithmic scale and its phase for SW modes excited in H-nanomagnet at saturation. The colorbar on the right of (b) quantifies the magnetization along the x-axis, whereas colorbar on the right of (c) quantifies the SW power and phase within the nanomagnet.	79

3.4	(a, b) 2D vector plot of the demagnetization field (top panel), effective magnetic field (middle panel), and underlying magnetic state (bottom panel) in an E-nanomagnet is shown at saturation (a) and at remanence (b), respectively. (c, d) Line plots of the in-plane and out-of-plane components of the demagnetization field and total effective field along the x-axis across the center of the nanomagnet, i.e., $y = 50$ nm.	80
3.5	(a, b) 2D vector plot of the demagnetization field (top panel), effective magnetic field (middle panel), and underlying magnetic state (bottom panel) in an H-nanomagnet is shown at saturation (a) and at remanence (b), respectively. (c, d) Line plots of the in-plane and out-of-plane components of the demagnetization field and total effective field along the x-axis across the center of the nanomagnet, i.e., $y = 150$ nm.	81
3.6	FFT power spectra of excited SW modes for (a) E-nanomagnet and (c) H-nanomagnet at remanence. (b, d) Spatial power and phase distribution of excited SW modes for E- and H-nanomagnet. The colorbars quantifying the power and phase are shown adjacent to their spatial profiles.	82
3.7	FFT power spectra of excited SW modes for dipolar coupled nanomagnets arranged in L-shape configuration at (a) remanence and (c) saturation. Insets on the right show the underlying energy-minimized spin configurations. The inset on the left of (a) shows the zoomed image of the weak SW modes at ~ 6.2 GHz. (b, d) Corresponding spatial power distribution of excited SW modes for this dipolar coupled nanomagnet arrangement at remanence and saturation. The colorbar quantifying the power on a logarithmic scale is shown on the right.	83
3.8	(a-e) Normalized magnetization (M_x/M_s) vs. external magnetic field ($\mu_0 H_{\text{ext}}$) curve for the ring studied ring type geometries: single, double, triple, quadruple (square ASI), and diag-double rings. Insets in the M - H curve show the different microstates stabilized during field sweep. These microstates are numbered as (i) and (ii), which appear as a result of two consecutive magnetization reversals in E-nanomagnets. (f) The underlying magnetization state at remanence is shown in the representation of macrospins. The colorbar on the right quantifies the magnetization component along the x-axis, i.e., the easy axis.	86
3.9	(a) Internal spin configuration in single and double ring structure prior and after the first observed steps in the M - H curve shown in Fig. 3.8(a, b).	87

3.10	SW power spectra of the studied ring type structures at saturated state. Zoomed spectra of the highlighted region in the left curve are shown on the right to visualize the presence of weak SW modes. Insets in the left curve represent the schematic of different ring-type geometries for which spectra are shown.	89
3.11	(a-e) Spatial distribution of power of excited SW modes in saturation for single, double, triple, quadruple (square ASI), and diag-double ring structures. For clarity, power is shown in a logarithmic scale, and a colorbar quantifying the power is shown in the bottom right corner.	90
3.12	(a) SW power spectra of the studied ring type structures at remanence. Zoomed spectra of the highlighted region in the left curve are shown on the right to clearly visualize the presence of weak SW modes. (b) Respective spatial power distribution of excited SW modes in logarithmic scale for a single square ring geometry.	92
3.13	(a, b) Normalized line power profile of SE mode along the easy axis of the upper and bottom E-nanomagnets of square single ring geometry at remanence for two different scales.	93
3.14	Spatial power distribution of excited SW modes in studied ring type structures viz., double, triple, quadruple (square ASI), and diag-double ring geometries at remanence. Here, the power of the mode is shown in dB (logarithmic scale). A colorbar on the bottom right corner quantifies the power of excited SW mode.	95
3.15	(a) SW spectra in state (i) i.e., magnetic state after 1 st switching in E-nanomagnets of ring type structures. (b) Corresponding spatial power distribution of excited SW modes in a square single ring. Here, the power of the mode is shown in dB (logarithmic scale). A colorbar on the bottom right corner quantifies the power of excited SW mode.	97
3.16	(a) Magnetic state after 1st magnetization reversal in upper E-nanomagnet of single ring (b) Bulk (B_E) SW mode excited in saturation and in state (i). The colorbar quantifies the power in dB as shown on the right.	99
3.17	(a-d) Spatial power distribution of SW modes excited in studied ring type structures viz., double, triple, quadruple (square ASI), and diag-double rings for state (i). Here, the power of the mode is shown in dB (logarithmic scale). A colorbar on the bottom right corner quantifies the power of excited SW mode.	100
3.18	(a-d) Spatial power distribution in bulk (B_E) SW modes excited in investigated ring type structures at saturation (first panel) and state-i (second panel). The magnetization state after magnetization reversal in E-nanomagnet at first observed switching is shown in the third panel of (a-d).	101

3.19	SW spectra of studied ring-type structures in state (ii), (b) Corresponding power profiles of the SW modes in single square ring structure in logarithmic scale (dB). A colorbar quantifying the power of excited SW modes in dB is shown in the bottom right corner.	103
3.20	Spatial power distribution of the excited SW modes in our studied ring-type structures for state (ii). Here, power distribution is shown in dB (logarithmic scale). A colorbar on the bottom right corner quantifies the power of excited SW mode.	104
3.21	(a-d) Top panel: underlying magnetization state in ring type structures after 1st (left) and 2nd (right) switching in E-nanomagnets. A colorbar quantifying the m_x component is shown in the middle right corner. Bottom panel: corresponding spatial power distribution of the switching identifier B_E mode excited at ~ 15 GHz in state (ii) at 14.9 GHz in saturation for respective ring-type structures. A colorbar on the bottom right corner is shown to quantify the power in dB (logarithmic scale).	106
4.1	(a) schematic illustrating the open-edge (OE) configuration of the square ASI system, featuring local transient field pulse excitation applied at the central vertex along the z-axis (out of the plane), and an external bias field applied in the XY plane at an angle θ relative to the x-axis. The inset below (a) displays the three-dimensional spatial profile of the local excitation. (b) Schematic representation of the closed-edge (CE) square ASI. (c) Representation of a transient square field pulse with a rise time (t_{rise}), fall time (t_{fall}), and duration (t_{dur}) each set at 20 ps. The nanomagnet dimensions for (a) and (b) are $300 \text{ nm} \times 100 \text{ nm} \times 30 \text{ nm}$, with an edge-to-edge inter-nanomagnet gap of 150 nm.	109
4.2	(a) Representative SW spectra (black solid line) for OE vertex at saturation, i.e., $H_{\text{ext}} = 200 \text{ mT}$ applied along the x-axis. Spectra for individual E-nanomagnets (red solid line) and H-nanomagnets (red dotted line). The inset shows the schematic diagram for applied field direction. (b) Internal spin configuration in the perpendicularly placed nanomagnets for $H_{\text{ext}} = 200 \text{ mT}$ as highlighted in the inset of (a).	112
4.3	(a-e) The power profile of the excited SW modes for open-edge vertices at saturation. The colorbar shows the FFT power of real-time oscillations of the z-component of magnetization in linear and logarithmic scales. (f) Schematic of the Cartesian coordinates indicating the easy axes of E- and H-nanomagnets.	114
4.4	(a) Schematic of OE-square ASI vertex with different cutlines shown as black and red dashed lines along the easy and hard axes of constituting nanomagnets. These cutlines are labeled as C1, C2, ..., and C6, respectively. (b-f) Line power profile of excited Sw modes in OE-square ASI vertex along the different cutlines shown in (a).	116

4.5	(a) SW spectra for the open-edge vertex at remanence depicted by the black solid line, when the initial bias field is applied along the x-axes. The spectra for individual nanomagnets are also shown at remanence with a red solid line, as illustrated in (a)). The bottom left provides a schematic illustrating the macrospin configurations at remanence. (b) Underlying magnetic state of OE vertex at remanence. Blue and red solid circles illustrate the local magnetic charges (Q_m) at outer type-III configured vertices.	119
4.6	(a) SW spectra of the dipolar coupled nanomagnets arranged in L-shaped geometry at remanence, featuring two magnetic state configurations: tail-to-tail, representing a magnetically charged state, and head-to-tail, representing a magnetically uncharged state. The insets provide visualizations of the magnetic states for both the tail-to-tail and head-to-tail configurations of the nanomagnets in the L-shaped geometry. (b) SW spectra of the single vertex geometry with predefined magnetization configurations, categorized as types I, II, III, and IV. The insets display the arrow diagrams illustrating the macrospin's configuration under investigation.	120
4.7	(a) Power spectra of OE vertex as a function of lattice constant (edge-to-edge separation: 100 to 500 nm) under transient field pulse excitation, the microstate of OE vertex for lattice constant at (b) 100 nm and (c) 500 nm.	122
4.8	(a-c) The power profile of the excited SW modes for open-edge vertex at remanence. The color bar shows the FFT power of real-time fluctuations of the z component of magnetization in linear and logarithmic scales.	123
4.9	Line scan of power profiles along the two orthogonal directions, as illustrated in the inset of (a), for the excited SW modes at (a) 6.4 GHz and (b) 10.4 GHz in the remanent state. The blue and red lines represent profiles along the x and y directions, respectively. The highlighted regions indicate nanomagnets at the central vertex that are subjected to pulse-field excitation.	124
4.10	Dispersion of the excited SW modes at remanence as a function of wave vector (k).	126
4.11	SW spectra for OE vertex at remanence when the initial magnetic field is applied at an angle 45° from the x-axis (easy axis of half of the nanomagnets). The top left inset shows the remanent magnetic state, depicting type-II spin configuration at each vertex, i.e., symmetric magnetically chargeless state. The bottom right inset shows the magnetic field configuration.	128

4.12	The power profile of the SE mode excited at 6.4 GHz (a) and the B mode excited at 10.4 GHz (b) at remanence for $\theta = 45^\circ$ is presented. Red color rings in (a) encircle the four outer vertices which are labeled as V1, V2, V3, and V4. Here, the red arrow in (b) represents the direction of an external field applied before reaching the remanent state. The blue dashed rectangular box encloses the nanomagnets positioned along the initial magnetic field orientation, whereas the red dashed rectangular box encloses the nanomagnets positioned along the transverse magnetic field orientation. Further, Q1, Q2, Q3, and Q4 denote the four quadrants segmenting the nanomagnets lying along the longitudinal and transverse field orientations. The color bar on the right indicates the FFT power of real-time fluctuations of the z-component of magnetization in dB.	129
4.13	(a) Schematic of OE-square ASI vertex with different cutlines shown as black and red dashed lines along the easy and hard axes of constituting nanomagnets. These cutlines are labeled as C1, C2, C4, and C5, respectively. (b-e) Line power profile of excited Sw modes in OE-square ASI vertex along the different cutlines shown in (a).	130
4.14	Line power profiles across the two orthogonal directions in the vertex V4 for the excited (a) SE and (b) B modes at remanence.	131
4.15	(a) SW spectra for OE vertex at remanence when the initial magnetic field is applied at an angle 135° from the x-axis (easy axis of half of the nanomagnets). The top left inset shows the remanent magnetic state, depicting type-II spin configuration at each vertex. The bottom right inset shows the magnetic field configuration. (b, c) Power profiles of the excited SW modes in logarithmic scale at 6.34 and 10.4 GHz, respectively. (d, e) Corresponding line scan of power profiles along the two orthogonal directions, i.e., C1 and C4 cutlines shown in the schematic of Fig. 4.13(a). Highlighted regions in (d, e) indicate nanomagnets at the central vertex that are subjected to pulse-field excitation.	133
4.16	(a) SW spectra for OE vertex at remanence when the initial magnetic field is applied at an angle 90° from the x-axis (easy axis of half of the nanomagnets). The top left inset shows the remanent magnetic state, depicting type-III spin configuration at two outer vertices and type-II spin configuration in the remaining vertices. The bottom right inset shows the magnetic field configuration. (b, c) Power profiles of the excited SW modes in logarithmic scale at 6.34 and 10.4 GHz, respectively. (d, e) Corresponding line scan of power profiles along the two orthogonal directions, i.e., C1 and C4 cutlines shown in the schematic of Fig. 4.13(a). Highlighted regions in (d, e) indicate nanomagnets at the central vertex subjected to pulse-field excitation.	134

4.17	(a) Power profile of the excited SW modes in logarithmic scale at 9.9 GHz. (b) Corresponding line scan of power profiles along the two orthogonal directions, i.e., C1 and C4 cutlines shown in the schematic of Fig. 4.13(a). Highlighted regions in (b) indicate nanomagnets at the central vertex that are subjected to pulse-field excitation.	135
4.18	The energy-minimized magnetic state of square ASI array at remanence when an initial bias field is applied along the easy axis of one of the sublattices, specifically at 0° (a) and at 45° (b) from the easy axis of one of the sublattices. The red and blue dots situated at the outer vertices within the blue highlighted region of (a) illustrate the charged vertices displaying a type-III macrospin configuration. The red and blue color coding in these field circles is employed to represent the net local diverging flux (Q_m) and converging flux ($-Q_m$), respectively.	136
4.19	SW spectra for a 5×5 vertex array for equilibrium magnetic states shown in Fig. 4.18 when initial magnetic field is applied at angles $\theta = 0^\circ$ and 45° , respectively	137
4.20	Profiles depicting the spatial power distribution in logarithmic scale of the excited SW modes corresponding to the microstates illustrated in panels (a, b) of Fig. 4.18, respectively. Highlighted regions in the power profile of 10.4 GHz SW mode exciting for $\theta = 45^\circ$ depict the nanomagnets aligned along the longitudinal and transverse magnetic field directions, respectively. A colorbar showing the power scale in dB is shown in the bottom right corner.	138
4.21	The line power profile of the bulk SW mode across the highlighted regions in Fig. 4.18 of square ASI array at remanence for (a) $\theta = 45^\circ$ and (b) $\theta = 0^\circ$. Here, θ denotes the angle subtended by the initial bias field at the easy axis, i.e., the x-axis, of one of the sublattices. In these panels, the red and blue lines represent the line power profiles along the horizontal and vertical directions, respectively, corresponding to the highlighted regions in panels (a) and (b) of Fig. 4.18. The highlighted regions in panels (a) and (b) correspond to the nanomagnets of the central perturbed vertex.	139
4.22	(a) Possible spin configurations in vertices of coordination number, $z = 1$ to 4. Arrow diagrams of magnetic charge cloud state (b) and monopole-polaron state. Note that the magnetization along the x, y axes are shown using black arrows, whereas magnetization along -x, -y axes is shown using red arrows. Vertices with net magnetic charges are illustrated by colorful magenta and violet boxes, whereas uncharged vertices are represented by gray boxes.	141
4.23	SW spectra in CE vertex for three different macrospins arrangement: magnetic monopole-polaron states, i.e., m-polaron I & II having different magnetic charge distribution at the edge mixed coordinated vertices ($z = 1, 3$), 3) and charge cloud state. Insets on the left and right depict this macrospins arrangement.	142

4.24	(a, b) The dependency of SW modes' frequency on the magnetic field is depicted as a 2D surface plot, along with a normalized magnetization (M_z) vs. bias field strength plot during the down-sweep for OE and CE-square ASI vertices. The power of the SW mode is represented in dB to enhance the visibility of weaker SW modes against the stronger ones, with the intensity displayed in a colorbar on the right. The white arrow indicates the direction of the bias field sweep (down-sweep). Insets in (a) and (b) provide schematics of OE and CE vertices. SW spectra for CE and OE vertices at remanence (c), and at $H_{\text{ext}} = 150$ mT (d) when the external bias field is applied along the easy axes of half of the nanomagnets is shown. An inset in (a) illustrates the macrospin arrangement and the presence of uncompensated charges at odd coordination vertices for the CE vertex at remanence.	144
4.25	Power profiles of the excited SW modes at (a) remanence and (b) $H_{\text{ext}} = 150$ mT applied along the x-axis for OE and CE vertices. (c, d) Macrospins configuration of underlying magnetic state for OE and CE vertices, respectively, at remanence. The insets on the bottom right corner of (b) show the colorbar and filed direction on the XY Cartesian plane. For $H_{\text{ext}} = 150$ mT, the equilibrium magnetization direction in each nanomagnet of the OE and CE vertices is pointed along the field direction, i.e., the x-axis.	146
5.1	Schematic depiction of (a) a single square ASI vertex and (b) a defective square ASI vertex with closed edges, presenting a tilted nanomagnet at 20° deviation from the y-axis. The dimensions of the nanomagnet are illustrated in the schematic. Scanning electron micrograph displaying the (c) square ASI vertex array and (d) defective square ASI vertex array with misaligned nanomagnets at alternating vertices. (e) Schematic representation of the TR-MOKE measurement configuration featuring an square ASI vertex as the sample.	152
5.2	Line plot shows the experimental TR-MOKE signal of the (a) reference permalloy ($\text{Ni}_{80}\text{Fe}_{20}$) film and (c) square ASI lattice. Corresponding fast Fourier transform of the TR-MOKE signal is shown in (b, d) for reference permalloy ($\text{Ni}_{80}\text{Fe}_{20}$) film and square ASI lattice, respectively. The magnetic component of the TR-MOKE signal and its corresponding FFT are shown in a black solid line, whereas the nonmagnetic component is shown in a red dashed line in the plot. The inset in (d) depicts the schematic of the square ASI configuration and applied field orientation.	155
5.3	Magnetic field dependence of the excited fundamental SW mode (red circular dots) for the reference permalloy film as measured from TR-MOKE spectroscopy. The Kittel fit of the experimentally measured signal is shown using a blue dashed line.	157

5.4	(a) Magnetic moment (M) as a function of the applied magnetic field ($\mu_0 H_{\text{ext}}$), measured for the reference permalloy film at room temperature using a SQUID magnetometer. Measurements were conducted with the magnetic field applied both in the IP and OOP orientation of the sample. (b) M - H within a small field range of ± 15 mT.	158
5.5	Normalized Fourier power spectra obtained from the measured Kerr (a) and reflectivity (b) signal, plotted against the external magnetic field for square ASI lattice. Identified dynamical modes are represented by distinct color markers on top of the 2D image plot in (a). The colorbars on the right of the 2D image plots show the intensity of the power spectra signal. The bottom left inset shown in (a) depicts the external magnetic field configuration in the square ASI lattice.	159
5.6	(a-b): Simulated geometry of the square ASI vertex composed of nanomagnets with sharp (a) and corrugated edges (b) as present in the fabricated (real) samples. Zoomed images of individual nanomagnets within the square ASI vertex are provided inside the red dashed box. The right panel displays the simulated magnetization state at remanence corresponding to each case. (c) AFM image of the square ASI vertex with its corresponding MFM image scanned at the remanent state is presented. Constituent nanomagnets are outlined with red dashed lines in the MFM image, and the magnetization in each nanomagnet is represented by arrows.	162
5.7	Magnetic field dependence of the simulated SW modes for square ASI vertex when edge corrugation is considered (a) and neglected (b) in the simulation geometry.	164
5.8	Simulated power profiles (top panel) and corresponding phase profiles (bottom panel) of the SW modes excited at frequencies of 9.5 and 16 GHz are depicted. The simulations are conducted under the influence of an external magnetic field of 192 mT applied along the x-axis. The colorbars on the right side of the figure are shown to quantify the power and phase.	165
5.9	(a) Temporal evolution of temperature associated with electron, lattice, and spin bath after the irradiation of laser pulse, computed utilizing the three-temperature model within COMSOL Multiphysics environment. The inset on the top right position illustrates a zoomed image of the temperature evolution within the first 5 ps. (b) Volume distribution of temperature of electron bath at $t = 2$ ps after laser pulse incident. A color bar indicating the temperature scale is presented on the right.	167

5.10	(a) Temporal evolution of the phonon bath (T_1) at three specific locations within the nanomagnet, denoted by black, red, and blue dots in the schematic of the nanomagnet shown in the inset at the bottom right corner. (b) Temperature distribution of T_1 , representing the lattice temperature profile across the thickness of the nanomagnet after 2 ps of the laser pulse irradiation. An inset in the bottom left corner illustrates the cut-line traversing the nanomagnet, along which the variation of T_1 is depicted.	170
5.11	(a) Temporal evolution of the displacement component (u_z) following the incidence of a laser pulse at the center of the top surface of the nanomagnet. (b) Spatial distribution of the volume displacement field at specific time instances, namely, $t = 4, 20, 36,$ and 300 ps, subsequent to the laser pulse incidence.	172
5.12	(a, b) Temporal evolution of the x and y components of the displacement field (u_x, u_y) following the incidence of a laser pulse at the center of the top surface of the nanomagnet.	172
5.13	(a) FFT power spectra of the time-varying displacement component (u_z), revealing the existence of multiple phonon (elastic) modes in the square ASI lattice. The inset in the top right corner illustrates the simulated geometry, highlighting a specific point location on the top surface of the nanomagnet where the displacement component is measured. (b) Representative time-response of the x, y, and z components of the calculated ME field at the same point location, computed from the time-varying magnetization and strain components.	173
5.14	Frequency response of the simulated ME modes (a) and experimentally observed modes (b) in TR-MOKE spectroscopy as a function of the applied magnetic field. Inset in (b) shows the unit cell of the simulated square ASI configuration, opted for the calculation of ME modes. The colorbar on the right shows the intensity of the power spectra signal.	174
5.15	(a) Measured frequency response of TR-MOKE signal as a function of the angle (θ) of applied magnetic field ($\mu_0 H_{\text{ext}} = 145 \text{ mT}$) for square ASI lattice is shown as 2D image plot. Identified dynamical modes that exhibit linear dispersion with field are shown as pink circular markers, whereas simulated dynamical modes exhibiting similar characteristics with field are shown concurrently by black and red diamond markers. The inset shows the schematic of the magnetic field configuration in the square ASI vertex. (b) The frequency response of the measured TR-MOKE signal against magnetic field amplitude for $\theta = 45^\circ$ is shown as a 2D image plot. Experimentally identified dynamical modes are shown in red circular dots on top of the 2D image plot, whereas simulated dynamical modes are shown in yellow diamond markers. The colorbar on the right shows the intensity of the power spectra signal.	176

5.16	(a) Simulated frequency response of excited SW modes as a function of the angle (θ) of applied magnetic field ($\mu_0 H_{\text{ext}} = 145 \text{ mT}$) for square ASI lattice is shown as 2D image plot. (b) The frequency response of the simulated SW modes against magnetic field amplitude for $\theta = 45^\circ$ is shown as a 2D image plot. The colorbar on the right shows the intensity of the power spectra signal. Note that these simulations are performed using the exact SEM geometry i.e., consideration of corrugated edges in the square ASI lattice.	177
5.17	Phonon mode spectrum of square ASI lattice for a magnetic field of amplitude 145 mT applied at an angle (θ) of 45° . The spectrum is calculated from the FFT of experimentally measured time-resolved reflectivity signal.	179
5.18	Line plot shows the experimental TR-MOKE signal of the (a) defective square ASI lattice. The corresponding fast Fourier transform of the TR-MOKE signal is shown in (b). The magnetic component of the TR-MOKE signal and its corresponding FFT are shown in a black solid line, whereas the nonmagnetic component is shown in a red dashed line in the plot. Inset in (b) depicts the SEM image of the defective square ASI configuration and applied field orientation. . . .	181
5.19	Normalized power spectra obtained from the measured Kerr (a) and reflectivity (b) signal, plotted against the external magnetic field for defective-square ASI lattice. Identified dynamical modes are represented by distinct color markers on top of the 2D image plot in (a). The colorbars on the right of the 2D image plots show the intensity of the power spectra signal. The bottom left inset shown in (a) depicts the external magnetic field configuration in the square ASI lattice. . .	183
5.20	Magnetic field dependence of the simulated SW modes for the defective-square ASI system when edge corrugation is considered (a) and neglected (b) in the simulation geometry.	185
6.1	Schematic of Co/Pt bilayer nanodisk subjected to an external magnetic field applied along the z-axis.	191
6.2	Response of (a) normalized magnetization (M_z/M_s) and (b) susceptibility (χ) along with topological charge (Q_t) during the downsweep of external magnetic field for Co/Pt circular nanodisk of diameter: 180 nm.	193

6.3	Representative 2-dimensional magnetization profiles of the observed magnetic states within their stability regime, as highlighted in Fig. 6.2. Here, white and black colors denote the spins pointing along the OOP direction, viz., $\pm z$ -axis, respectively. Other colors represent magnetization in the nanodisk plane. A color wheel on the left indicates the direction of magnetization in the plane. The respective line profiles of the reduced magnetization components ($M_{x,y,z}/M_s$) across the geometrical center of the nanodisk are shown below each respective magnetization image.	194
6.4	(a) Magnetization profile of the novel magnetic state as a 2-dimensional quiver plot. The color of the arrows is associated with different spin orientations in the plane of the nanodisk, as opted from the color wheel shown in the bottom right corner. White and Black colors denote the spin orientation along the OOP direction ($\pm z$ -axis), respectively. (b) Cross-sectional view of the spin configuration across the geometrical center of the nanodisk (radial direction, i.e., x-axis). (c, d) Line profile of the OOP and IP magnetization components across the geometrical center as extracted from (a). (e) Schematic of the magnetization vector and its polar and azimuthal angle shown in cartesian plane. (f) Line profile of the azimuthal angle of the magnetization vector across the geometrical center, i.e., along the x-axis as calculated from (c) and (d). (g, h) Spatial distribution of the IP and OOP magnetization components of this novel magnetic state. The colorbars on the right denote the magnitude of the respective magnetization components.	197
6.5	Formation of different magnetic state configurations as a function of the magnetic field in Co/Pt nanomagnet of diameter (D) varying from 140 to 260 nm.	199
6.6	(a) Representative SW power spectra of the observed chiral textures at intermediate field strength within their respective field regimes: (top) for RV (290 mT), E-SKY (130 mT), SKYm (-135 mT) & E-SKYm (-140 mT), and (bottom) for the novel magnetic state (-275 mT). The insets in the top right corner show the zoomed images of the spectra for the frequency range of 15 to 17.5 GHz (top) and 2.1 to 11 GHz (bottom) to highlight the presence of weaker SW modes in the chiral textures. The inset in the bottom right corner shows the spectrum for the HS state (170 mT).	202
6.7	2-dimensional spatial distribution of power and phase of the SW modes (shown in Fig. 6.6) along with their respective line power (LP) profiles across the geometrical center below each spatial power distribution image of (a-e). The colorbars indicating the power and phase of SW modes are shown on the right.	206

6.8	(a-c) 2-dimensional spatial distribution of the phase of the excited SW modes (shown in Fig.6.7) in RV, E-SKY, and novel magnetic state along with their respective line power (LP) profiles across the geometrical center below each spatial phase distribution image.	207
6.9	(a-c) Top: the line profile illustrates the magnetization oscillations in the δm_z component across the geometrical center (radial direction) resulting from sinusoidal magnetic field wave excitation at SW resonance frequencies of a radial vortex (RV) state (290 mT). The profile is shown at distinct time instances with a time-stepping of $1/f$. The blue dotted line represents the z-component of normalized magnetization in the equilibrium state ($t = 0$). The zero axis for both norm. M_z and δm_z is shown using a red dotted horizontal line. Bottom: the image (surf plot) below each line profile displays the snapshot of instantaneous magnetization oscillation in the Co/Pt nanomagnet. The colorbar in copper indicates the time parameter, while the BWR (blue-white-red) colorbar represents the amplitude of the magnetization oscillation.	208
6.10	(Left) The line profile illustrates the magnetization oscillations in the δm_z component across the geometrical center (radial direction) resulting from sinusoidal magnetic field wave excitation at SW resonance frequencies of a SKY state (-130 mT). The profile is shown at distinct time instances with a time-stepping of $1/f$. The blue dotted line represents the z-component of normalized magnetization in the equilibrium state ($t = 0$). The zero axis for both norm. M_z and δm_z is shown using a red dotted horizontal line. (Right) The image (surf plot) below each line profile displays the snapshot of instantaneous magnetization oscillation in the Co/Pt nanomagnet. The copper colorbar indicates the time parameter, while the BWR (blue-white-red) colorbar represents the amplitude of the magnetization oscillation.	209
6.11	(a, b) Top: the line profile illustrates the magnetization oscillation in the δm_z component across the geometrical center (radial direction) resulting from sinusoidal magnetic field wave excitation at SW resonance frequencies of a skyrmionium (-135 mT). The profile is shown at distinct time instances with a time-stepping of $1/f$. The blue dotted line represents the z-component of normalized magnetization in the equilibrium state ($t = 0$). The zero axis for both norm. M_z and δm_z is shown using a red dotted horizontal line. Bottom: the image (surf plot) below each line profile displays the snapshot of instantaneous magnetization oscillation in the Co/Pt nanomagnet. The copper colorbar indicates the time parameter, while the BWR (blue-white-red) colorbar represents the amplitude of the magnetization oscillation.	210

- 6.12 (a-c) Top: the line profile illustrates the magnetization oscillation in the δm_z component across the geometrical center (radial direction) resulting from sinusoidal magnetic field wave excitation at SW resonance frequencies of an E-SKYm state (-140 mT). The profile is shown at distinct time instances with a time-stepping of $1/f$. The blue dotted line represents the z-component of normalized magnetization in the equilibrium state ($t = 0$). The zero axis for both norm. M_z and δm_z is shown using a red dotted horizontal line. Bottom: The image (surf plot) below each line profile displays the snapshot of instantaneous magnetization oscillation in the Co/Pt nanomagnet. The copper colorbar indicates the time parameter, while the BWR (blue-white-red) colorbar represents the amplitude of the magnetization oscillation. 211
- 6.13 (a-c) top: the line profile illustrates the magnetization oscillations, i.e., δm_z , across the geometrical center (radial or x-direction) resulting from sinusoidal magnetic field excitation at frequencies of excited SW modes for a novel magnetic state (-275 mT). Magnetization oscillations are shown at distinct time instants with a time-stepping of $3/10f$. The blue dotted line represents the z-component of normalized magnetization in the equilibrium state ($t = 0$). The copper colorbar on the right indicates the time parameter, while the BWR (blue-white-red) colorbar at the bottom represents the magnitude of the magnetization oscillations (δm_z). The zero axis for both norm. M_z and δm_z is shown using a red dotted horizontal line. (bottom) Snapshot of the corresponding instantaneous magnetization oscillation in the Co/Pt nanodisk. 214
- 6.14 (a) The average magnetization oscillation (δm_z) resulting from a sinusoidal magnetic field at a frequency of 0.8 GHz, applied along the z-axis, indicates the transition from a novel magnetic state to a SKY state. The inset depicts the magnetization configuration before and after the transition caused by the sinusoidal magnetic field application. (b) The average magnetization oscillation (δm_z) resulting from a sinusoidal magnetic field application at a frequency of 2.5 GHz, applied along the z-axis, indicates the transition from a skyrmionium to a novel magnetic state. The inset depicts the magnetic configuration before and after the transition caused by the sinusoidal field application. 215
- 6.15 The frequencies of excited SW modes vs. $\mu_0 H_{\text{ext}}$ during downsweep of the external magnetic field. The static properties, including topological charge and susceptibility, of these states are presented below. . 217

7.1	SEM image of bi-component pinwheel ASI (a) with defects, namely misaligned nanomagnet, and (b) without defects. The dimension of the wider nanomagnet here is 600,nm × 200,nm × 25,nm, whereas the dimension of the narrow nanomagnet is 600,nm × 120,nm × 25,nm. The angle of misalignment of the misaligned nanomagnet is 10° from its original easy axis. Zoomed scans of (a, c) are shown in (b, d). . . .	224
7.2	(a) An optical image depicting the fabricated device used for magnetotransport studies of the ASI lattice. (b) A corresponding SEM image illustrating the fabricated device. (c) A SEM image displaying the region where the ASI configuration is fabricated using EBL. (d-f) SEM images showing the three distinct ASI configurations composed of ferromagnetic permalloy nanowires. . . .	225

List of Tables

3.1	External magnetic field strengths at which different microstates are stabilized via magnetization reversal in E-nanomagnets.	85
3.2	Frequency and nature of excited SW modes in state-I i.e., state after magnetization reversal in E-nanomagnets corresponding to switching-(i)	98
3.3	Frequency and nature of excited SW modes in state-II i.e., state after magnetization reversal in E-nanomagnets corresponding to switching-(ii)	102
4.1	Frequency of excited SW modes in CE vertex at different possible microstates	142
4.2	Frequencies of excited SW modes in OE and CE vertex at an external magnetic field of 150 mT.	144
5.1	laser and material parameters employed in the heat transfer module for three temperature simulation ASI vertex.	169
5.2	The employed material parameters for the elastic simulations in the solid mechanics module of COMSOL Multiphysics.	171
6.1	Frequencies of excited SW modes in different chiral magnetic states observed for $D = 180$ nm.	201
6.2	Characteristics of SW modes excited for different chiral magnetic states as observed from the power and phase distribution shown in Fig.6.8. See Table6.1 for the mode frequencies. Here ‘Y’ and ‘N’ denote ‘Yes’ and ‘No’, respectively.	205

Abbreviations

SW	S pin W ave
FFT	F ast F ourier T ransformation
FDM	F inite D ifference M ethod
FDTD	F inite D ifference T ime D omain
FEM	F inite E lement M ethods
ASI	A rtificial S pin I ce
OE	O pen E dge
CE	C losed E dge
SE	S hort E dge
LE	L ong E dge
B	B ulk
LLG	L andau L ifshitz G ilbert
MC	M agnonic C rystal
DMI	D zyaloshinskii M oriya I nteraction
EA	E asy A xis
STNO	S pin T orque N ano O scillator
EBL	E lectron B eam L ithography
AFM	A tomio F orce M icroscopy
MFM	M agnetic F orce M icroscopy
SEM	S canning E lectron M icroscopy
EDS/EDX	E lectron D ispersioe X -ray S pectroscopy
EBD	E lectron B eam D eposition
SQUID	S canning Q uantum I nterference D evice
TR-MOKE	T ime R esolved M agneto O ptic K err
ME	M agneto E lastic
CMOS	C omplementary M etal O xide S emiconductor

Abbreviations

HM	H ea v y M etal
FM	F erromagnet M etal
CW	C lock W ise
CCW	C ounter C lock W ise
FMR	F erromagnetic R esonance
PEEM	P hoto E lectron E mission M icroscopy
AC	A lternating C urrent
SAW	S urface A coustic W ave
BDF	B ackward D ifferentiation F ormula
PMA	P erpendicular M agnetic A nisotropy
CV	C harged V ertex

Symbols

M	magnetization vector
M_S	saturation magnetization
D_{ij}	DM vector
α	Gilbert damping coefficient
H_{eff}	effective magnetic field vector
$\frac{\partial \mathbf{M}}{\partial t}$	rate of change of magnetization vector
γ	gyromagnetic ratio
F	magnetic free energy
U	internal energy
S	entropy
G	Gibbs free energy
μ_0	magnetic permeability
B	magnetic flux
E_Z	Zeeman energy
J	exchange coupling constant
ϕ_{ij}	angle between adjacent spins
A	exchange constant
E_{BIL}	bi-linear exchange energy
H_{dip}	dipolar field
H_d	demagnetization field
E_{ms}	magnetostatic energy
E_{ani}	anisotropy energy
K	anisotropy constant
K_u	uniaxial anisotropy constant
H_k	anisotropy field
α_i	direction cosines

Symbols

\mathbf{N}_{ij}	dimensionless demagnetization tensor
θ	polar angle of magnetization vector
ϕ	azimuthal angle of magnetization vector
ω	frequency of magnetization oscillation
\mathbf{E}	electric field vector
\mathbf{D}	electrical displacement vector
Q_v	Voigt constant
ε_{ij}	elastic strain
σ_{pq}	Cauchy stress tensor
u_i	displacement
E	Young's modulus
ν	Poisson ratio
λ, μ	Lamé parameters
λ_S	saturation magnetostriction
B_1, B_2, A_1, A_2	magnetoelastic constants
c_{ij}	elastic moduli
U_{MEL}	magnetoelastic energy
H_{MEL}	magnetoelastic field
Q_t	topological charge
m	unit vector of magnetization
S_i	spin in a magnet
T	temperature
T_C	Curie temperature
r	position in a material
R	reflectivity
ϵ	dielectric constant/permittivity
k_0	wavevector in free space
n_{eff}	effective index
ω	angular frequency
λ	wavelength
n_i	refractive index
k	spring constant